Micron 92 (2017) 13–18

Contents lists available at ScienceDirect

Micron

journal homepage: www.elsevier.com/locate/micron

In situ tracking the reversible spinel-rocksalt structural transformation between Mn_3O_4 and MnO

Xingyuan San, Bo Zhang*, Jing Wang, Bo Wu, Xiuliang Ma

Shenyang National Laboratory for Materials Science, Institute of Metal Research, Chinese Academy of Sciences, Wenhua Road 72, 110016 Shenyang, China

ARTICLE INFO

Article history:
Received 29 July 2016
Received in revised form
18 September 2016
Accepted 18 September 2016
Available online 27 October 2016

Keywords:
In-situ transmission electron microscopy
Mn_3O_4
Reversible transformation
Beam irradiation

ABSTRACT

Electron beam irradiation is well known to induce damage in materials. The structural transformation involved in the damage is usually believed to be an irreversible solid state chemical reaction. Here we use in situ transmission electron microscopy (TEM) combined electron-energy loss spectroscopy (EELS) technique in an aberration-corrected TEM to track the structural transformation in spinel Mn_3O_4 induced by electron beam irradiation. It is clarified that spinel Mn_3O_4 is transformed to rocksalt structured MnO by irradiation and the reversed recovering transition from rocksalt MnO to spinel Mn_3O_4 can occur by aging in the gentle electron beam circumstance. The mechanisms including the role of O desorption/adsorption and the displacement of Mn and O involved in the reversible transformation processes are discussed. The work presents an implication that electron beam can modify the structure at atomic dimension yielding diverse assemblies of surfaces, interfaces and colorful properties.

1. Introduction

The AB_2O_4 spinel structures exhibit unusual physical, chemical and rheological properties (Radaelli et al., 2002; Liang et al., 2011; Karato et al., 1998), thus attracting much attention from the scientific community for many years. In spinel transition metal oxides, Mn_3O_4, due to its low-cost, environmental benignity, and unusual property, is a good candidate as pervasive application material (Seo et al., 2004; Wang et al., 2010; Li et al., 2014). The refined structure of Mn_3O_4 has been intensively studied experimentally, especially the oxidation states of Mn in the distorted spinel structure of Mn_3O_4 (Xiao et al., 2004; Tan et al., 2011). Of particular importance the atomic resolution elemental mapping has become feasible over the past years by means of spatially resolved electron-energy loss spectroscopy (EELS) with high-angle annular dark field (HAADF) technique in an aberration-corrected electron microscope (Tan et al., 2011; Yu et al., 2010). However, the manganese oxide compound has found to be extremely sensitive to damage by the electron beam in the transmission electron microscopy (TEM), especially in the STEM-EELS experiments performed at 300 kV. The behavior of manganese oxide compounds under electron beams is also important for energy application (Phillips et al., 2014; Lin et al., 2014). Previous studies paid little attention on the reversible transformation of manganese oxide compounds (Phillips et al., 2014; Lin et al., 2014), even believed the transformation induced by the electron beam irradiation is an irreversible solid state chemical reaction (Pennycook et al., 2014). Here, we report an interesting reversible spinel-rocksalt structural phase transition between Mn_3O_4 and MnO under electron irradiation.

2. Experimental

The well-shaped spinel Mn_3O_4 nano-octahedral particles were prepared by the hydrothermal method (Li et al., 2011). A drop of the solution containing the Mn_3O_4 powders was dripped on holey carbon films which supported on a copper mesh grid, then dried for further TEM observation. The TEM specimen was observed initially and recorded the original structural feature. Then the electron beam was focused to irradiate the small edge region with the electron flux of near 9×10^5 A/m^2. During the irradiating process, the beam-induced structural evolution was monitored and recorded. Finally, the focused beam was spread to the electron flux of below 4×10^5 A/m^2, yielding the specimen keeping aging in the gentle electron beam circumstance and the resulting structural evolution being monitored.

The HRTEM and HAADF-STEM experiments were performed in a Titan Cubed 60–300 kV aberration-corrected TEM fitted with a high-brightness field-emission gun (X-FEG) and double Cs corrector operating at 300 kV. The EELS spectra were acquired using Gatan Image Filter (GIF, Quantum 965) with the Dual-EELS acquisition

* Corresponding author.
E-mail address: bozhang@imr.ac.cn (B. Zhang).

http://dx.doi.org/10.1016/j.micron.2016.09.008
0968-4328/

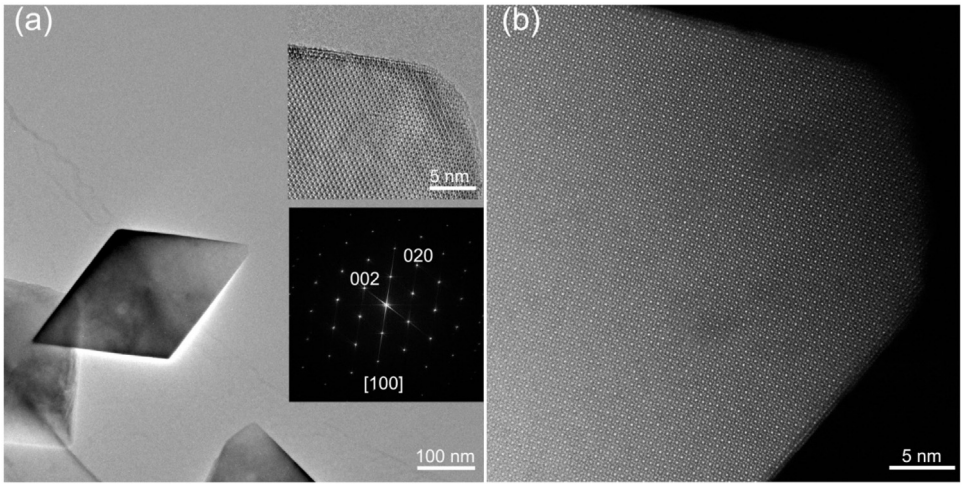

Fig. 1. Characterization on the as-synthesized Mn_3O_4 particles. (a) Low-magnification bright-field TEM image showing a typical rhombus shape of projection along [100] direction of a spinel octahedral-shape Mn_3O_4 nanoparticle. Insets are the HRTEM and the FFT images. (b) High resolution HAADF-STEM image along [100] zone axis showing the typical atom projection arrangement of spinel. It can be seen that the particle has the sharp and well-defined edge and the homogeneous structure from surface to interior.

mode. The probe convergence semi-angle was approximately 21.4 *m*rad. An energy dispersion of 0.25 eV/channel and 0.1 eV/channel was used and the energy resolution of the system was roughly 1.8 eV and 1.2 eV, respectively. In order to avoid adopting the unreliable signals induced by the contingent beam damage during the EELS experiments, we acquired and compared the two images from the same region before and after scanning to ensure free of damage.

3. Results and discussion

3.1. The structure evolution induced by the electron irradiation

Fig. 1a is a low-magnification TEM image, showing the nano-sized Mn_3O_4 particle has a well-defined octahedral shape. The HRTEM image (Fig. 1a, inset) and the HAADF-STEM image (Fig. 1b) along the [100] direction show the perfectly sharp edge, and the Fast Fourier transform (FFT) (Fig. 1a, inset) of the HRTEM image can be indexed to be the tetragonal Mn_3O_4 structure with the space group $I4_1/amd$. The Mn_3O_4 TEM specimen was irradiated by a focused electron beam with a constant current density of about 9×10^5 A/m^2 for some duration and then was tracked the irradiation induced structural evolution. The high resolution HAADF-STEM image is shown in Fig. 2a and the zoom-in image is shown in Fig. 2b. The [100] crystal direction is frequently chosen because the Mn^{2+} (in Purple) and Mn^{3+} (in Green) cations are separated in different atomic columns, and the Mn^{2+} atoms are located at the 8a tetrahedral sites in the lattice while the Mn^{3+} atoms are located on the 16d octahedral site (Tan et al., 2011). It is evident that the rocksalt structure was nucleated at the edge of the Mn_3O_4, which indicates that electron beam induces the transformation of spinel Mn_3O_4 to rocksalt structure yielding the formation of the reconstruction skin layer. Interestingly, in-situ HRTEM experiment was recorded in video 1 in the Supplementary material, which clearly shows the evolution process of crystal structure. The orientation relationship is rocksalt structure [110]//Mn_3O_4 [100] and rocksalt structure (-110)//Mn_3O_4 (010), as indicated in the FFT inset. Fig. 2c shows the EELS full spectra, which were obtained from the bulk and the reconstruction region respectively. Fig. 2d shows the enlarged view of the O-K edge, where the prepeak structure of the O-K edge can be interpreted in terms of transition processes governed by the dipole selection rule (Kurata and Colliex, 1993). Fig. 2e shows the enlarged view covering the Mn-$L_{2,3}$ edges. Compared with the bulk, the Mn-L_2 and L_3 edges corresponding to the reconstruction region are found to shift towards the lower energy loss, which indicates the decrease in the average oxidation state of transition metal cations at the surface. Besides that, with the method of double arctangent and the Pearson method (Van Aken et al., 1998; Pearson et al., 1993; Wang et al., 2000; Tan et al., 2012), the white-line intensity ratio I (L_3)/I (L_2) for the bulk and the surface is calculated to be roughly 2.8 and 3.6, respectively. The higher I (L_3)/I (L_2) ratio is another indicator of a lower valance on the surface transformed layer. The lower oxidation state of manganese should be bivalent manganese and thus the rocksalt structured reconstruction layer is identified to be MnO.

It is noteworthy that people usually focus on the decomposition and reduction from the high oxidation states to low oxidation states for transition metal oxides. For examples, V_2O_5, TiO_2, MoO_3 and Nb_2O_5 would transform to rocksalt structure suboxides by electron irradiation (Su and Schlögl, 2002; Wang et al., 2004; Smith et al., 1987; Xu et al., 1993). The damage induced by irradiation usually is believed to be an irreversible process (Pennycook et al., 2014). Interestingly, by aging, we observed that the transformed rocksalt structured MnO can recover to the original spinel structured Mn_3O_4 and thus concluded that the damage indeed is a reversible process. After irradiating the specimen for some duration, the electron beam was spread and thus the specimen was aged in the friendly gentle beam circumstance. Then we monitored the structure evolution.

Fig. 3a is the HAADF image showing the evolution of the rocksalt structured transformed layer after aging for about 5 min. The observed region is the same place with that shown in Fig. 2a. It is seen that a very small region at the outmost surface has recovered to the spinel structure as marked with white circle. Further aging for half an hour, the transformed region has almost recovered to the spinel structure except a very small middle zone keeping rocksalt structure as marked with red circle in Fig. 3b. This is in accordance with the in-situ HRTEM observation recorded in the simplified video 2 in the Supplementary material. It is shown that the recover process goes from outside to inside. The enlarged view of the sandwich-like region is shown in Fig. 3c, where three regions marked with the white circles are chosen to perform the EELS analysis and the spectra are shown in Fig. 3d. Since the material is quite electron beam sensitive, relatively low doses and quick acquirement time are necessary. Compared with the spectra of the bulk region 1, the evident chemical shift, as expected, is clearly observed in the region 2, and doesn't occur in the recovered region 3. Evi-

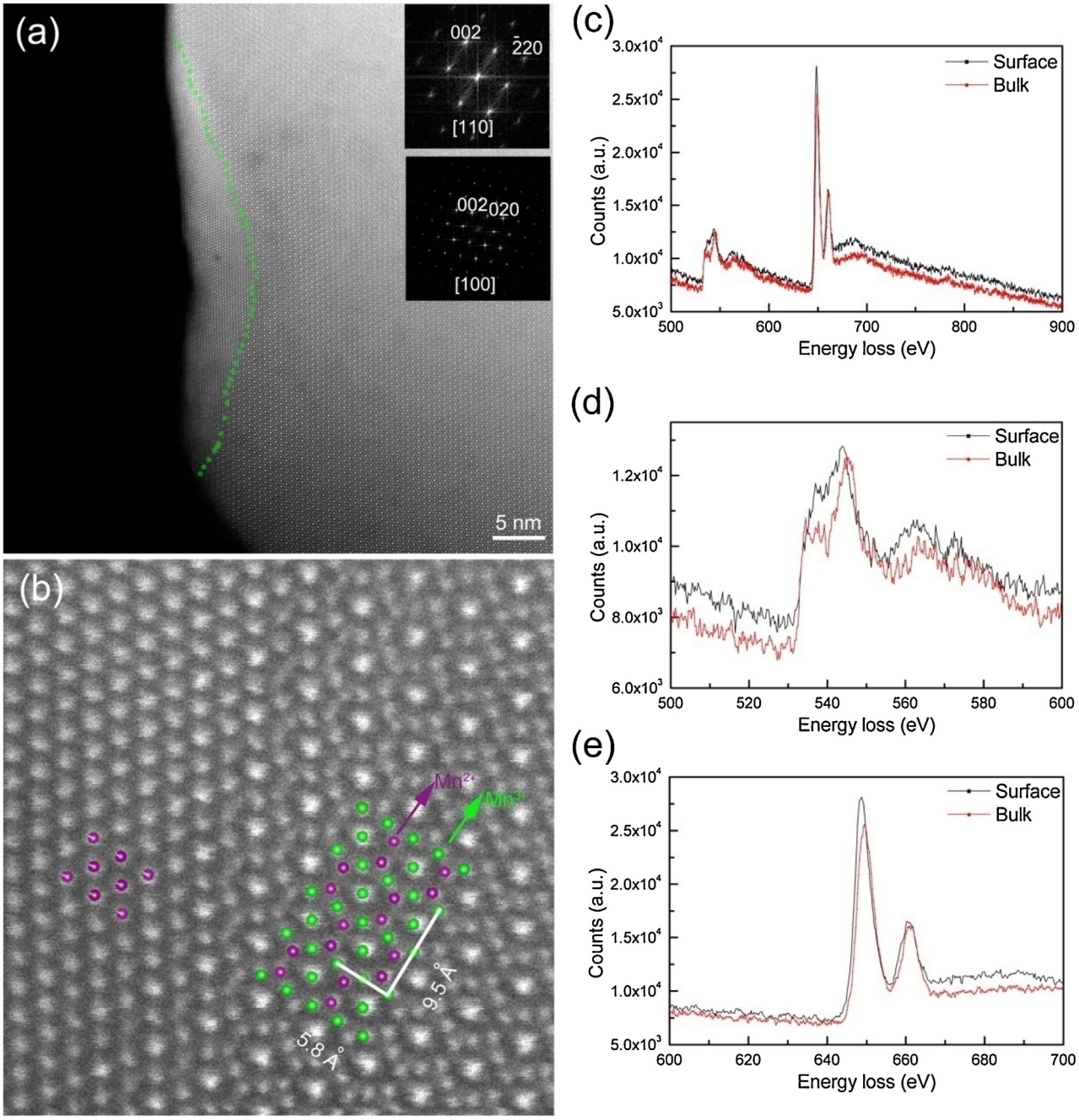

Fig. 2. The structural transformation in Mn_3O_4 induced by electron beam irradiation. (a) High-resolution HAADF-STEM image after irradiation by the focused electron beam with current density of about 9×10^5 A/m^2. A transformed skin layer with different atomic columns arrangement is well defined as marked with green dash line. Insets are FFT images taken from the bulk region and the transformed layer. (b) The enlarged view of an illustrating the representations of the atom columns. The Mn (III) cation columns highlighted in green dots and the Mn (II) cation columns highlighted in purple dots. (c–e) The EELS analysis on the bulk and the transformed layer of the Mn_3O_4: the full spectra covering the EELS edges from O to Mn (c); detail views with enlarged scale of O K-edges (d) and Mn-$L_{2,3}$ edges (e). The chemical shift to lower energy loss for the transformed zone is evident. (For interpretation of the references to colour in this figure legend, the reader is referred to the web version of this article.).

dently, aging in a gentle dose of current can recover the damage leading to the formation of the spinel Mn_3O_4 again.

Evidently, the reversible transition involves a redox chemical reaction as follows:

$$\text{Reductionreaction}: Mn_3O_4 \rightarrow 3MnO + 1/2O_2 \quad (1)$$

$$\text{Oxidationreaction}: 3MnO + 1/2O_2 \rightarrow Mn_3O_4 \quad (2)$$

$$\text{Thebalancedreaction}: 3MnO + 1/2O_2 \rightleftarrows Mn_3O_4 \quad (3)$$

For the oxidation reaction (2), the standard molar Gibbs energy variation ΔG° is calculated to be $-194.5\,\text{kJ mol}^{-1}$, which means the oxidation of MnO to Mn_3O_4 is a spontaneous process thermodynamically and can undergo in air without beam irradiation. Indeed, we observed the transition in air at room temperature with a relatively lower rate than that in gentle beam circumstance.

3.2. *The mechanisms of the irradiation induced reduction: $Mn_3O_4 \rightarrow MnO$*

There are various kinds of radiation damages according to the type of electron scattering and the effects produced in a specimen, such as electrostatic charging, ionization damage (radiolysis) and

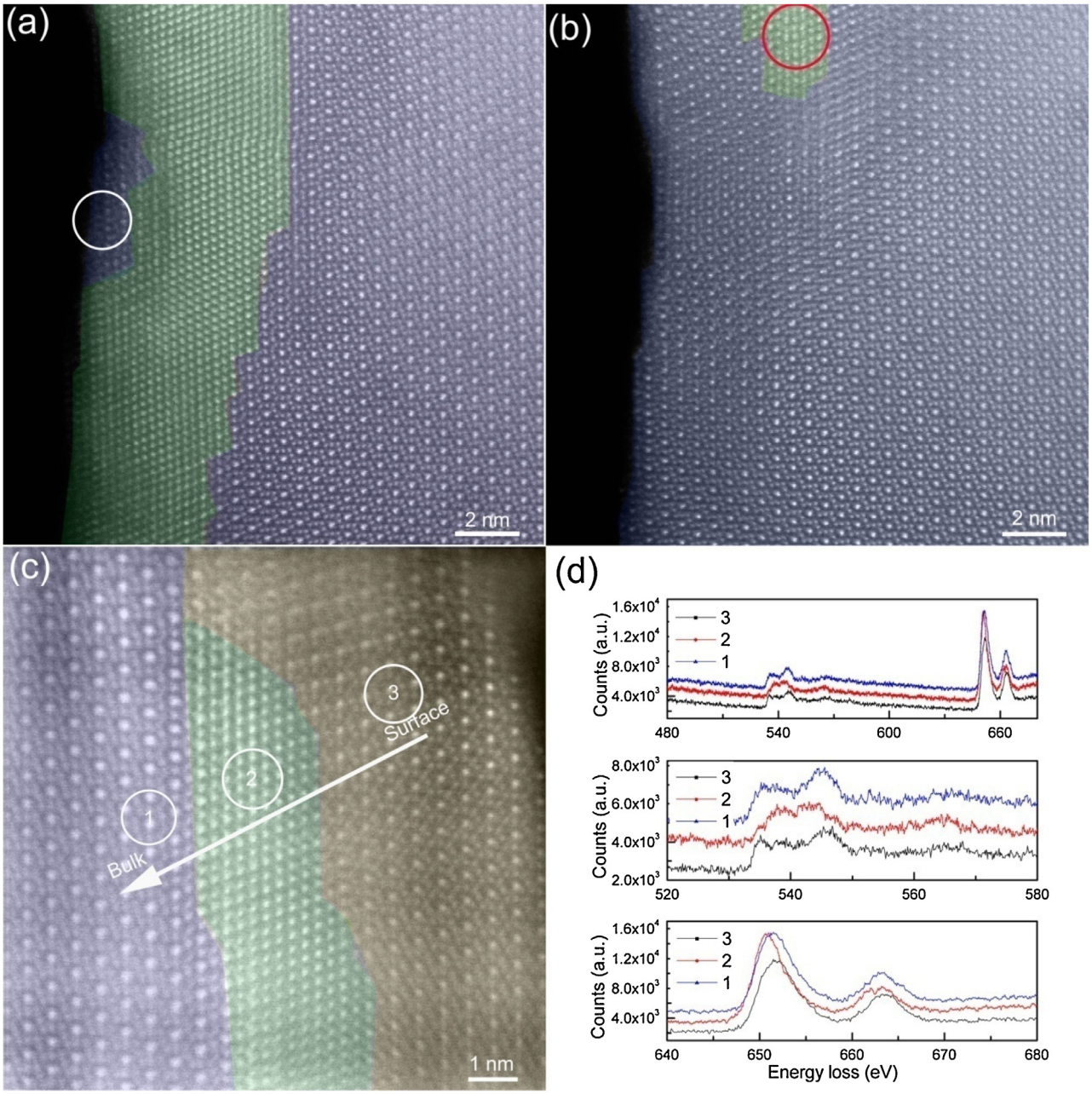

Fig. 3. The reversed recovery transformation from MnO to Mn_3O_4. High resolution HAADF-STEM image showing the evolution of the rocksalt structured transformed layer after aging for about 5 min (a) and 30 min (b). (c) Zoom-in image containing the bulk region (circle 1), transformed layer (circle 2) and the recovery layer (circle 3). (d)The EELS analysis on the three regions marked with the circles.

displacement damage (Egerton et al., 2004). The maximum energy (E_{max}) transferred from the irradiated electron beam can be calculated by the simplified equation (Pennycook et al., 2014; Egerton et al., 2004):

$$E_{max} = \frac{2E_0}{Mc^2}(E_0 + 2m_0c^2) \quad (4)$$

where M is the nuclear mass, E_0 is the energy of the incident electron, m_0 is the electron mass, and c is light velocity. The E_{max} transferred from the incident electron accelerated by the voltage of 300 kV is calculated to be 15.5 eV, much greater than the required 10 eV to displace Mn atom in bulk crystal (Pennycook et al., 2014; Egerton et al., 2010). The current density is another important factor for radiation damage. The dose rate of 9×10^5 A/m^2 is high enough for elastic (electron-nucleus) and even inelastic (electron-electron) scattering. Currently, above-mentioned mechanisms of damage are possible reasons for this transformation during irradiation, such as O loss from lattice (Phillips et al., 2014), atom motion and displacement (Pennycook et al., 2014; Jiang, 2013). The detailed process of the O loss from lattice and motion will be described later.

3.3. *The mechanisms of the irradiation catalyzed oxidation: $MnO \rightarrow Mn_3O_4$*

3.3.1. *The interfacial and electron beam heating effect*

The Mn_3O_4 has a spinel structure with lattice parameters a = 5.76 Å and c = 9.47 Å. The rocksalt structured MnO has a lattice constant of 4.44 Å. There is a large lattice mismatch of 9% along the MnO [110] direction, yielding the mismatch misfit strain and thermal stress (Zhan et al., 2002) as possible inducements for the

rocksalt-spinel transition. Considering the experimental phenomena that the recovering transition goes from outside to inside rather than at interface, the transition from MnO to Mn_3O_4 should not be governed by the mismatch strain. Meanwhile, another phenomenon that the MnO has a slower transition rate in the air atmosphere at room temperature, indicates that the recovering transition process could be temperature dependent. Usually, the temperature rise (ΔT) with electron-beam heating can be calculated according to Fisher's mode (Fisher, 1970; Zheng et al., 2013),

$$\Delta T = \frac{I}{\pi\kappa e}\left(\frac{\Delta E}{d}\right)Ln\frac{b}{r_0} \quad (5)$$

where I is the beam current, k is the thermal conductivity, e is the electron charge, b is the sample radius, r_0 is the beam radius, and ΔE is the total energy loss per electron in a sample with a thickness of d. The maximum temperature rise is estimated to be roughly less than 3 K with I = 9.4 nA, b = 1.5 mm, r_0 = 100 nm, dE/dx = 730MeV/m (which was roughly calculated from the Bethe-Bloch equation) (Zheng et al., 2013; Utsunomiya et al., 2003), and k = 10 W/mK (Slack and Newman, 1958). Such a little increase of 3 K should not be responsible for the accelerated recovery process, which is in agreement with other studies that the temperature increase due to e-beam heating is negligible (Bae et al., 2007; Wang et al., 2007). Thus, the electron beam heating effect could be excluded for the present case. There is another experimental phenomenon to confirm the negligible e-beam heating effect. According to the Eq. (5), the temperature rise is heavily dependent on the current, not the current density (Jiang, 2015). However, the recovery transition rate was found to strongly current density dependent below the threshold in TEM mode. The same tendency was also found in the STEM mode that the MnO has a slower transition rate at the spot size 9 than (lower current density) at the spot size 6 (higher current density).

3.3.2. The desorption, adsorption and diffusion of oxygen

In fact, the reversible transformation can be mainly related to the two parts: the oxygen desorption/adsorption (O releasing/taken from/to the lattice) and oxygen diffusion (the displacement of Mn and O). In the first part, at high dose rate, charge density can be very high. The charged layers produce strong electric fields at the surface region. Then electric field pumps the O^{2-} ions in the lattice toward the surfaces, forms O_2, and sublimated from surfaces (Jiang, 2015), which corresponds to the electron beam induced reduction process. At low dose rate, the electric field can provided electrons to dissociate O_2 molecules (come from the vacuum system of the TEM instrument) at the oxide surface via the following reaction: $O_2 + e^- \rightarrow O^- + O$ (Coad et al., 1970; Collot et al., 1985), yielding the creation of adsorbed oxygen anions and then to be taken to the lattice, which corresponds to the electron beam accelerated oxidation process. Another part of oxygen diffusion can involve the surfaces mass transport process (Wang et al., 2007) and ionization-induced processes (Bae et al., 2007). According to the Eq. (4), the maximum amount of energy transferred to O nuclei by a 300 kV e-beam is roughly 54 eV. The threshold displacement energy for O in most oxides falls at the values of more than 40 eV (Wang et al., 2007). The creation of oxygen and manganese vacancies would be driven by the knock-on displacement in here. Higher current density means higher electron bombardment rate, leading to disordering of ions and the formation of point defects such as vacancies and interstitial sites, which accelerates the ions diffusion. Another possible route is the ionization-induced processes, which was found to play an important role in recrystallization in many works (Bae et al., 2007; Meldrum et al., 1997a,b). The ionization processes involving the breaking or rearrangement of unstable bonds (Meldrum et al., 1997a,b) also produced O vacancies (Jiang, 2015). So, the electron beam-induced defect-mediated transport process can directly responsible for the electron-beam-flux dependent transition rate. There should be a critical beam current density which 'controlled' the atomic motion and reversible transformation. If the current density is higher than the critical value, oxygen would be desorbed from the surface of the sample (Jiang, 2015) or excited by the electron beam yielding the damaging process (Mn_3O_4 to MnO). On the contrary, if it is lower than the critical value, oxygen would adsorb, and then be accelerated to diffuse on the sample yielding the recovering process (MnO to Mn_3O_4). Certainly, it's worth further investigating the mechanism in the future study to see how changing and re-changing by various beam current densities and varied ways.

Interfaces are major research topic in materials science with special emphasis on reduced dimensions in the case of applications of nano-materials. The various structures lead to various properties, especially between the Mn_3O_4 and MnO, such as the magnetic of antiferromagnetic MnO nanoparticles with shells of ferrimagnetic Mn_3O_4 (Berkowitz et al., 2008). An important implication of the present work is that precisely controlling the electron beam can modify the surface and interface at the nanometer even atomic dimensions to obtain diverse assemblies of interfaces and surfaces yielding colorful properties.

4. Conclusion

With application of in situ TEM combined with EELS technique, we have succeeded to track the structural evolution at atomic scale in the spinel Mn_3O_4 nanoparticles induced by electron beam irradiation. Spinel-to-rocksalt transition was induced by the focused electron beam irradiation and the reversed transition would occur when aging in the spread gentle electron beam circumstance. The transition layer is determined to be the rocksalt structured MnO. The threshold value of the current density is assumed to determine the transition direction above which the damage process of spinel-to-rocksalt transition occurs involving O releasing from the lattice and below which the recovering process of rocksalt-to-spinel transition occurs involving O taken to the lattice. The work presents an important implication that colorful properties created by diverse assemblies of surfaces and interfaces can be accomplished by electron beam modification at a nanometer or even atomic scale.

Acknowledgements

This work is supported by the National Natural Science Foundation of China (51101157), the Innovation Fund in IMR (SCJJ-2013-PY-09).

Appendix A. Supplementary data

Supplementary data associated with this article can be found, in the online version, at http://dx.doi.org/10.1016/j.micron.2016.09.008.

References

Bae, I.T., Zhang, Y.W., Weber, W.J., Higuchi, M., Giannuzzi, L.A., 2007. Electron-beam induced recrystallization in amorphous apatite. Appl. Phys. Lett. 90, 21912.
Berkowitz, A.E., Rodriguez, G.F., Hong, J.I., An, K.J., Hyeon, T., Agarwal, N., Smith, D.J., Fullerton, E.E., 2008. Antiferromagnetic MnO nanoparticles with ferrimagnetic Mn_3O_4 shells: doubly inverted core-shell system. Phys. Rev. B 77, 024403.
Coad, J.P., Bishop, H.E., Riviere, J.C., 1970. Electron-beam assisted adsorption on Si(111) surface. Surf. Sci. 21, 253–264.
Collot, P., Gautherin, G., Agius, B., Rigo, S., Rochet, F., 1985. Low-pressure oxidation of silicon stimulated by low-energy electron-bombardment. Philos. Mag. B 52, 1051–1069.
Egerton, R.F., Li, P., Malac, M., 2004. Radiation damage in the TEM and SEM. Micron 35, 399–409.
Egerton, R.F., McLeod, R., Wang, F., Malac, M., 2010. Basic questions related to electron-induced sputtering in the TEM. Ultramicroscopy 110, 991–997.

Fisher, S.B., 1970. On the temperature rise in electron irradiated foils. Radiat. Eff. 5, 239–243.
Jiang, N., 2013. Damage mechanisms in electron microscopy of insulating materials. J. Phys. D: Appl. Phys. 46, 305502.
Jiang, N., 2015. Electron beam damage in oxides: a review. Rep. Prog. Phys. 79, 016501.
Karato, S.I., Dupas-Bruzek, C., Rubie, D.C., 1998. Plastic deformation of silicate spinel under the transition-zone conditions of the Earth's mantle. Nature 395, 266–269.
Kurata, H., Colliex, C., 1993. Electron-energy-loss core-edge structures in manganese oxides. Phys. Rev. B 48, 2102.
Li, Y., Tan, H.Y., Yang, X.Y., Goris, B., Verbeeck, J., Bals, S., Colson, P., Cloots, R., Van. Tendeloo, Su, G.B.L., 2011. Well shaped Mn_3O_4 nano-octahedra with anomalous magnetic behavior and enhanced photodecomposition properties. Small 7, 475–483.
Li, G.M., Tang, X.B., Lou, S.Y., Zhou, S.M., 2014. Large enhancement of ferromagnetism by Cr doping in Mn3O4 nanowires. Appl. Phys. Lett. 104, 173105.
Liang, Y.Y., Li, Y.G., Wang, H.L., Zhou, J.G., Wang, J., Regier, T., Dai, H.J., 2011. Co_3O_4 nanocrystals on graphene as a synergistic catalyst for oxygen reduction reaction. Nat. Mater. 10, 780–786.
Lin, F., Markus, I.M., Doeff, M.M., Xin, H.L., 2014. Chemical and structural stability of lithium-ion battery electrode materials under electron beam. Sci. Rep. 4, 5694.
Meldrum, A., Boatner, L.A., Ewing, R.C., 1997a. Displacive radiation effects in the monazite-and zircon-structure orthophosphates. Phys. Rev. B 56, 13805.
Meldrum, A., Boatner, L.A., Ewing, R.C., 1997b. Electron-irradiation-induced nucleation and growth in amorphous $LaPO_4$, $ScPO_4$, and zircon. J. Mater. Res. 12, 1816–1827.
Pearson, D.H., Ahn, C.C., Fultz, B., 1993. White lines and d-electron occupancies for the 3d and 4d transition metals. Phys. Rev. B 47, 8471.
Pennycook, T.J., Jones, L., Pettersson, H., Coelho, J., Canavan, M., Mendoza Sanchez, B., Nicolosi, V., Nellist, P.D., 2014. Atomic scale dynamics of a solid state chemical reaction directly determined by annular dark-field electron microscopy. Sci. Rep. 4, 7555–7555.
Phillips, P.J., Iddir, H., Abraham, D.P., Klie, R.F., 2014. Direct observation of the structural and electronic changes of Li_2MnO_3 during electron irradiation. Appl. Phys. Lett. 105, 113905.
Radaelli, P.G., Horibe, Y., Gutmann, M.J., Ishibashi, H., Chen, C.H., Ibberson, R.M., Koyama, Y., Hor, Y.S., Kiryukhin, V., Cheong, S.W., 2002. Formation of isomorphic Ir3+ and Ir4+ octamers and spin dimerization in the spinel $CuIr_2S_4$. Nature 416, 155–158.
Seo, W.S., Jo, H.H., Lee, K., Kim, B., Oh, S.J., Park, J.T., 2004. Size-dependent magnetic properties of colloidal Mn_3O_4 and MnO nanoparticles. Angew. Chem. Int. Ed. 43, 1115–1117.
Slack, G.A., Newman, R., 1958. Thermal conductivity of MnO and NiO. Phys. Rev. Lett. 1, 359.
Smith, D.J., McCartney, M.R., Bursill, L.A., 1987. The electron-beam-induced reduction of transition metal oxide surfaces to metallic lower oxides. Ultramicroscopy 23, 299–303.
Su, D.S., Schlögl, R., 2002. Thermal decomposition of divanadium pentoxide V_2O_5: towards a nanocrystalline V_2O_3 phase. Catal. Lett. 83, 115–119.
Tan, H.Y., Turner, S., Yücelen, E., Verbeeck, J., Van Tendeloo, G., 2011. 2D atomic mapping of oxidation states in transition metal oxides by scanning transmission electron microscopy and electron energy-loss spectroscopy. Phys. Rev. Lett. 107, 107602.
Tan, H.Y., Verbeeck, J., Abakumov, A., Van Tendeloo, G., 2012. Oxidation state and chemical shift investigation in transition metal oxides by EELS. Ultramicroscopy 116, 24–33.
Utsunomiya, S., Yudintsev, S., Wang, L.M., Ewing, R.C., 2003. Ion-beam and electron-beam irradiation of synthetic britholite. J. Nucl. Mater. 322, 180–188.
Van Aken, P.A., Liebscher, B., Styrsa, V.J., 1998. Core level electron energy-loss spectra of minerals: pre-edge fine structures at the oxygen K-edge. Phys. Chem. Miner. 25, 494–498.
Wang, Z.L., Bentley, J., Evans, N.D., 2000. Valence state mapping of cobalt and manganese using near-edge fine structures. Micron 31, 355–362.
Wang, D., Su, D.S., Schlögl, R., 2004. Electron beam induced transformation of MoO_3 to MoO_2 and a new phase MoO. Z. Anorg. Allg. Chem. 630, 1007–1014.
Wang, C.M., Baer, D.R., Amonette, J.E., Engelhard, M.H., Antony, J.J., Qiang, Y., 2007. Electron beam-induced thickening of the protective oxide layer around Fe nanoparticles. Ultramicroscopy 108, 43–51.
Wang, H.L., Cui, L.F., Yang, Y., Sanchez Casalongue, H., Robinson, J.T., Liang, Y.Y., Cui, Y., Dai, H.J., 2010. Mn_3O_4- graphene hybrid as a high-capacity anode material for lithium ion batteries. J. Am. Chem. Soc. 132, 13978–13980.
Xiao, Y.N., Wittmer, D.E., Izumi, F., Mini, S., Graber, T., Viccaro, P.J., 2004. Determination of cations distribution in Mn_3O_4 by anomalous x-ray powder diffraction. Appl. Phys. Lett. 85, 736.
Xu, P., Dunn, D., Zhang, J.P., Marks, L.D., 1993. Atomic imaging of surfaces in plan view. Surf. Sci. 285, L479–L485.
Yu, R., Hu, L.H., Cheng, Z.Y., Li, Y.D., Ye, H.Q., Zhu, J., 2010. Direct subangstrom measurement of surfaces of oxide particles. Phys. Rev. Lett. 105, 226101.
Zhan, Q., Yu, R., He, L.L., Li, D.X., Li, J., Xu, S.Y., Ong, C.K., 2002. Reversible structural transition in epitaxial manganite film. Phys. Rev. Lett. 88, 196104.
Zheng, H., Liu, Y., Cao, F., Wu, S.J., Jia, S.F., Cao, A.J., Zhao, D.S., Wang, J.B., 2013. Electron beam-assisted healing of nanopores in magnesium alloys. Sci. Rep. 3, 1920.